Experimental evidence of a phase transition in the multifractal spectra of turbulent temperature fluctuations at a forest canopy top

Sylvain Dupont, Françoise Argoul, Evgeniya Gerasimova-Chechkina, Mark R. Irvine, Alain Arneodo

J. Fluid Mech. (2020), *vol.* 896, A15.
Published by Cambridge University Press
doi:10.1017/jfm.2020.348

Experimental evidence of a phase transition in the multifractal spectra of turbulent temperature fluctuations at a forest canopy top

S. Dupont[1,†], F. Argoul[2], E. Gerasimova-Chechkina[3], M. R. Irvine[1] and A. Arneodo[2]

[1]INRAE, Bordeaux Sciences Agro, ISPA, F-33140 Villenave d'Ornon, France

[2]Laboratoire Ondes et Matière d'Aquitaine, CNRS UMR5798, Université de Bordeaux, 33405 Talence, France

[3]Laboratory of Physical Foundation of Strength, Institute of Continuous Media Mechanics UB RAS, Perm, Russia

(Received 6 December 2019; revised 14 March 2020; accepted 27 April 2020)

Ramp–cliff patterns visible in scalar turbulent time series have long been suspected to enhance the fine-scale intermittency of scalar fluctuations compared to longitudinal velocity fluctuations. Here, we use the wavelet transform modulus maxima method to perform a multifractal analysis of air temperature time series collected at a pine forest canopy top for different atmospheric stability regimes. We show that the multifractal spectra exhibit a phase transition as the signature of the presence of strong singularities corresponding to sharp temperature drops (respectively jumps) bordering the so-called ramp (respectively inverted ramp) cliff patterns commonly observed in unstable (respectively stable) atmospheric conditions and previously suspected to contaminate and possibly enhance the internal intermittency of (scalar) temperature fluctuations. Under unstable (respectively stable) atmospheric conditions, these 'cliff' singularities are indeed found to be hierarchically distributed on a 'Cantor-like' set surrounded by singularities of weaker strength typical of intermittent temperature fluctuations observed in homogeneous and isotropic turbulence. Under near-neutral conditions, no such a phase transition is observed in the temperature multifractal spectra, which is a strong indication that the statistical contribution of the 'cliffs' is not important enough to account for the stronger intermittency of temperature fluctuations when compared to corresponding longitudinal velocity fluctuations.

Key words: atmospheric flows, fractals, intermittency

1. Introduction

Central to biosphere–atmospheric exchanges, a scalar advected by a turbulent flow in the atmospheric surface layer, the so-called scalar turbulence, has been the subject of increasing research interest at the frontiers of different disciplines of

† Email address for correspondence: Sylvain.Dupont@inrae.fr

the geosciences and the environmental sciences, including meteorology, climatology, hydrology, oceanography and ecology (Sreenivasan 1991; Katul *et al.* 2013). In particular, scalar turbulence at the vegetation canopy–atmosphere interface has attracted a great deal of attention in the past decades (Finnigan 2000; Harman & Finnigan 2008; Belcher, Harman & Finnigan 2012), as it explains heat and mass exchanges between the canopy and the above atmosphere.

Compared to surface boundary-layer flow, canopy flow (velocity) shows some similarities with a plane mixing-layer flow resulting from the interaction between a slower and a faster flow, within and above the canopy, respectively, where Kelvin–Helmholtz instabilities develop, reducing the flow anisotropy (Raupach, Finnigan & Brunet 1996; Katul & Chang 1999). Hence, canopy turbulence is a combination of mixing-layer-type coherent structures scaling with the vorticity thickness at the canopy top, surface-layer-type coherent structures whose length scales vary with distance from the surface and residual small wake eddies developing behind canopy elements (Poggi *et al.* 2004; Dupont & Patton 2012). Near the canopy top, velocity fluctuations exhibit scale invariance from scales smaller than the mixing-layer-type coherent structures where turbulence is produced, to scales larger than the dissipation scale; while deeper within the canopy, this scale invariance is often weakened by the presence of specific-scale wake eddies developing behind canopy geometries with a dominant length scale such as a tree trunk diameter (Poggi *et al.* 2004; Cava & Katul 2008; Dupont *et al.* 2012). With thermal instability, the canopy-top wind shear is weakened, and the shear-driven eddies are progressively replaced by buoyantly driven eddies in unstable conditions or damped in stable stratification (Dupont & Patton 2012).

Similar to scalar turbulence in common turbulent flows, the time series of active and passive scalar fields collected near the canopy top (e.g. temperature, particle or chemical species concentration, etc.) show both a larger intermittency at fine scales as compared to the longitudinal wind velocity (Schmitt *et al.* 1996), and the ubiquitous presence of ramp–cliff patterns (Paw U *et al.* 1992; Katul *et al.* 2006, 2013). The larger intermittency manifests itself by more intense and sporadic scalar fluctuations at small scales, leading statistically to a larger spectrum of singularities (multifractals), therefore contradicting the famous Kolmogorov (Kolmogorov 1941)–Obukhov (Obukhov 1949)–Corrsin (Corrsin 1951) (KOC) universal scaling of scalar fluctuations at high moment order q, i.e. for large fluctuations. The ramp–cliff patterns refer to gradual rises (respectively decreases) with weak scalar fluctuations over scales commensurate with the canopy height, followed by relatively sharp drops (respectively jumps) depending on whether the canopy is a source (respectively a sink) of the scalar under consideration. These structures have been the subject of intensive research due to their significant contribution to scalar turbulent fluxes (Gao, Shaw & Paw U 1989; Katul *et al.* 2013). Initially interpreted as the signature of convective plumes (Taylor 1958), these ramp–cliff patterns have been systematically observed from field and numerical experiments irrespective of the sign of the thermal stability, and whether the canopy is a source or a sink of the scalar (Gao *et al.* 1989; Paw U *et al.* 1992; Fitzmaurice *et al.* 2004). These patterns appear related to the coherent structures developing at the canopy top, corresponding to the anisotropic forcing of scalar fluctuations. By analogy with the surface renewal theory (Higbie 1935), a ramp–cliff pattern observed in scalar time series is interpreted as the result of a parcel of fluid coming from the above bulk fluid that remains in contact with the canopy top where scalar sources (sinks) are located, increasing (decreasing) progressively the amount of scalar in the fluid parcel, before being replaced by another fluid parcel (Paw U *et al.* 1995; Katul *et al.* 2006).

These ramp–cliff patterns are usually invoked as the possible cause of the larger fine-scale intermittency of scalar turbulence (Sreenivasan 1991; Sreenivasan & Antonia 1997; Shraiman & Siggia 2000; Warhaft 2000; Falkovich, Gawedzki & Vergassola 2001; Katul *et al.* 2003; Zorzetto, Bragg & Katul 2018), and thus the breakdown of the KOC scaling law of scalar fluctuations. Direct numerical simulations (Frisch, Mazzino & Vergassola 1998; Celani *et al.* 2000; Celani, Mazzino & Vergassola 2001; Iyer *et al.* 2018) and laboratory experiments (Warhaft 2000; Moisy *et al.* 2001) have further evidenced the role of cliff structures in saturating the scaling exponent of scalar fluctuations to a constant value for high moment order q, the so-called phenomenon of intermittency saturation. Hence, conversely to the traditional picture of the scale by scale cascade of energy from the large-scale anisotropic forcing (integral scale) to the viscous dissipation scale, with a rapid loss of the forcing anisotropic character during the process, in the presence of ramp–cliff structures, it is often suggested that the cascading process may be short circuited with some coupling between large and small scales, the latter still carrying some signature from the forcing scale (Katul *et al.* 2003; Zorzetto *et al.* 2018).

Despite considerable theoretical (Lvov, Procaccia & Fairhall 1994; Chertkov 1997; Pumir, Shraiman & Siggia 1997; Yakhot 1997; Balkovsky & Lebedev 1998; Falkovich *et al.* 2001), numerical (Meneveau, Lund & Cabot 1996; Higgins, Parlange & Meneveau 2003; Watanabe & Gotoh 2004; Xu *et al.* 2014) and experimental efforts (Sreenivasan 1991; Frisch 1995; Sreenivasan & Antonia 1997; Pope 2000; Warhaft 2000; Moisy *et al.* 2001), some debate remains concerning the statistical contribution of the ramp–cliff structures to the scalar intermittency at fine scales. In particular, an important issue left open is, to which extent these coherent structures indeed contribute to the larger deviation from the KOC universal scaling of the structure function exponent of scalars compared to that of the longitudinal velocity, larger deviation indicating a more intermittent scalar bulk turbulence field. In other words, does the presence of ramp–cliff patterns in scalar signals explain the larger intermittency at fine scales of the scalar fluctuations compared to that of the longitudinal velocity fluctuations?

Here, the impact of ramp–cliff structures on the fine-scale intermittency of scalar fluctuations is experimentally investigated using a high-frequency air temperature (θ) measured at the top of a forest canopy for different thermal stratifications, and compared with the intermittency of the longitudinal velocity fluctuations (u) recorded at the same location. To that purpose, a multifractal analysis of the θ and u signals is performed in order to characterize the scaling properties of θ and u fluctuations according to the magnitude of the fluctuations (moment order), and to highlight the strength of the strongest singularities (cliff) across scales. The signal singularities are located using a wavelet transform and the statistical singularity strengths are deduced from the slopes of the local maxima of the wavelet transform modulus across scales using the wavelet transform modulus maxima (WTMM) method.

The structure of the paper is as follows. In § 2, the measurements and multifractal analysis are described. In § 3, the multifractal characteristics (scaling exponents, singularity spectra) of the air temperature (θ) and longitudinal velocity (u) at canopy top are compared for different stability regimes, with observation of the saturation of the scaling exponent of θ for high moment order and non-neutral conditions. Then, in § 4, we discuss this saturation behaviour in regards to the presence of cliff singularities in the signal, suggesting an analogy with an ordered–disordered phase transition at a critical moment order, where the ordered phase is dominated by 'cliff' singularities and the disordered phase by a large spectrum of singularity strengths.

The absence of saturation in near-neutral conditions while θ fluctuations are still more intermittent than u fluctuations leads us to conclude that the statistical contribution of the 'cliffs' is not significant enough to explain the stronger intermittency of θ fluctuations. Finally, in § 5 the outcomes of the study are summarized and concluding remarks presented.

2. Material and method

2.1. *Measurements*

The air temperature and the three wind velocity components were measured during the summer 2016 within the atmospheric surface layer, near the top of a maritime pine forest ($z = 9.85$ m), using a three-dimensional sonic anemometer (Gill R3) sampling at 20 Hz. The forest plot was located at the Salles Integrated Carbon Observation Station (ICOS) (44°29′ N, 0°57′ W), in Les Landes region, in southwestern France. The forest was characterized by a mean tree height of $h = 8.4$ m and a leaf area index of approximately 3.2. This latter parameter indicates a canopy sufficiently dense to induce a mixing-layer-type flow at its top. The ground surface was flat in all directions, and the forest was wide enough to have negligible fetch effect in all wind directions. The recorded wind velocity components were rotated horizontally so that the longitudinal velocity (u) represents the horizontal component along the mean wind direction. To account for a possible error in the vertical orientation of the sonic anemometer, a second rotation was performed around the transverse axis to ensure a zero mean vertical velocity (w). The air temperature (θ) was deduced from the sonic anemometer speed of sound.

Following standard quality controls, a total of 27 time series (runs), of 2^{17} data points each (∼109 min), were selected for both θ and u. These runs covered different thermal stratifications, also referred to as stability regimes, ranging from unstable, near neutral to stable conditions, where the stability was defined from the stability parameter $\zeta = z/L$ at the canopy top, as commonly used in atmospheric surface-layer studies. Here, L is the Obukhov length (Obukhov 1946) defined as $L = -u_*^3 T/(\kappa g \overline{w'T'})$, where u_* is the friction velocity characterizing the momentum absorbed by the vegetated surface, T is the air temperature, g the gravitational acceleration and $\overline{w'T'}$ the kinematic sensible heat flux; L characterizes the height above which buoyant production (or destruction) of turbulent kinetic energy dominates the mechanical production. The sign of L reflects the direction of the heat flux, positive for daily unstable conditions with an upward heat flux, and negative for nocturnal stable conditions with a downward heat flux. In near-neutral conditions, the thermal stratification of the atmosphere is negligible and $|L| \to \infty$, leading to $|\zeta| \to 0$. For the range of stability conditions considered here, the mechanical production of turbulence is expected to always dominate the buoyant production or destruction.

To both investigate high-order moments and preserve turbulence stationarity, a time series length compromise of ∼109 min was reached. The time series included approximately 200 to 1400 integral scales of u and θ (L_u and L_θ, respectively) and 2300 to 7000 integral scales of w (L_w), varying with the stability. The wavelet transform of the signals was performed with the third derivative of the Gaussian wavelet, as described further, to remove the signal large-scale trends (third-order polynomial trends). To further ensure the similarity of turbulent eddies along the time series and their stationarity, we only kept those with a small variability of ζ. Unstable and stable runs were also selected under clear sky conditions and at the same time during the day, around midday and early night, respectively, to keep close radiation forcing and atmospheric boundary-layer conditions for runs of the same stability.

The Taylor hypothesis of frozen turbulence is usually applied to local point measurements to convert temporal to spatial scales (Kaimal & Finnigan 1994), assuming that velocity fluctuations are much smaller than the mean velocity of the main eddies (U_c), i.e. $\sigma_u^2/U_c^2 << 1$ with σ_u the standard deviation of the longitudinal velocity (Lin 1953). Even if the well-known mixing-layer-type flow prevailing at the canopy top leads to velocity fluctuations of the same order as the mean wind velocity (U_h), the mean convection velocity of the main eddies (U_c) is larger than U_h, $U_c \approx 1.8\,U_h$ (Raupach *et al.* 1996), which extends the validity the Taylor hypothesis at the canopy top (Kaimal & Finnigan 1994). The squared turbulence intensity relative to the squared convection velocity varies from 0.04 in stable conditions up to 0.18 for the most unstable runs (table 1), reaching the limit of applicability of the Taylor hypothesis for these latter runs. To overcome this limitation, we normalized the time scale with L_w (the integral scale of the vertical velocity w) (Zorzetto *et al.* 2018), assuming that the distortion of the main advected eddies impacted similarly the time scale and L_w, L_w being much smaller than L_u (table 1).

The ratio between the integral scales of u and w (L_u/L_w) is approximately 7.5, exhibiting the anisotropy of the large-scale wind motions at the canopy top, and is intermediate between the expected values in surface-layer and mixing-layer flows (Katul & Chang 1999). This value of 7.5 is close to the ratio observed by Katul & Chang (1999) for a pine forest, showing the generality of our canopy flow.

2.2. *Multifractal analysis*

The WTMM method was used to perform the multifractal analysis. This method has proved very efficient in estimating scaling exponents and singularity spectra of complex non-stationary time series related to various research areas, including fully developed turbulence (Muzy, Bacry & Arneodo 1994; Arneodo, Manneville & Muzy 1998*c*; Arneodo, Muzy & Sornette 1998*d*; Delour, Muzy & Arneodo 2001; Arneodo *et al.* 2002; Audit *et al.* 2002; Arneodo *et al.* 2003; Khalil *et al.* 2006; Arneodo *et al.* 2008; Roland *et al.* 2009; Roux *et al.* 2009; Arneodo *et al.* 2011). Compared to the structure function method, the WTMM method allows one to extract the entire range of non-oscillating singularities (cusp type) present in the signal provided that the wavelet is sufficiently smooth and localized in time and frequency, and with a sufficient number of vanishing moments (Muzy, Bacry & Arneodo 1993). Oscillating singularities (chirp type) are not expected or are negligible in our turbulence data as confirmed by Lashermes *et al.* (2008) and Abry, Roux & Jaffard (2011) on wind-tunnel turbulence data.

The strengths of the singularities of the wind velocity and air temperature signals f were computed from their wavelet transform (WT). The WT can be compared to a mathematical microscope (Muzy, Bacry & Arneodo 1991; Muzy *et al.* 1994; Arneodo, Bacry & Muzy 1995) whose lenses are a family of wavelets ψ with different zooming factors, characterized by the scale parameter a, which are shifted along the signal with a translation parameter b. The WT is well suited for the analysis of complex non-stationary time series such as those found in the atmosphere. The continuous wavelet transform of the function $f(t)$ is defined as

$$T_\psi[f](b,a) = \frac{1}{|a|}\int f(t)\overline{\psi}\left(\frac{t-b}{a}\right)\mathrm{d}t, \tag{2.1}$$

where f is here either u or θ, $T_\psi[f](b,a)$ is the wavelet coefficient that characterizes the degree of correlation between the signal f and the wavelet at the location b and

Run	ζ	L	U_h	u_*	H	σ_u^2/U_c^2	σ_w	σ_θ	L_u	L_w	L_θ	$D(h=0)$	q_{crit}
1	-1.13 ± 0.26	−9.0	0.9	0.31	314.0	0.18	0.43	1.02	27.23	5.10	19.32	0.00 ± 0.05	3.4
2	-0.59 ± 0.17	−17.9	1.4	0.41	393.7	0.17	0.56	1.11	27.83	2.78	9.43	0.10 ± 0.05	2.9
3	-0.53 ± 0.12	−19.5	1.3	0.37	259.1	0.12	0.51	0.84	15.56	2.92	8.28	0.10 ± 0.05	2.7
4	-0.52 ± 0.13	−19.9	1.4	0.39	289.1	0.13	0.50	0.91	15.17	2.81	9.14	0.35 ± 0.05	1.8
5	-0.33 ± 0.32	−50.7	1.6	0.55	367.4	0.13	0.61	0.94	12.23	1.88	11.48	0.15 ± 0.05	2.6
6	-0.31 ± 0.10	−34.1	1.3	0.39	162.7	0.12	0.47	0.53	15.67	2.75	16.86	0.00 ± 0.05	3.7
7	-0.29 ± 0.06	−34.6	1.9	0.52	394.9	0.11	0.64	1.06	12.47	1.94	11.17	0.37 ± 0.05	1.7
8	-0.29 ± 0.09	−35.8	1.7	0.51	366.4	0.14	0.61	0.99	19.06	2.22	7.03	0.30 ± 0.05	2.0
9	-0.27 ± 0.05	−37.6	1.8	0.52	364.5	0.12	0.65	0.96	22.65	1.82	8.06	0.40 ± 0.05	1.6
10	-0.26 ± 0.19	−58.8	2.1	0.60	392.3	0.10	0.67	1.00	8.56	1.37	9.15	0.10 ± 0.05	3.0
11	-0.25 ± 0.10	−47.7	2.1	0.53	301.1	0.12	0.64	0.92	16.99	1.52	16.42	0.32 ± 0.05	2.4
12	-0.19 ± 0.04	−54.6	2.0	0.59	368.2	0.12	0.68	0.98	8.76	1.85	7.72	0.16 ± 0.05	2.0
13	-0.16 ± 0.04	−62.9	2.2	0.65	405.3	0.10	0.70	1.03	7.66	1.41	14.64	0.49 ± 0.05	1.4
14	-0.16 ± 0.02	−64.1	1.9	0.57	265.7	0.10	0.61	0.78	8.88	1.53	12.98	0.15 ± 0.05	2.9
15	-0.15 ± 0.04	−68.5	1.6	0.41	93.2	0.10	0.46	0.39	11.52	2.10	15.44	—	—
16	-0.15 ± 0.10	−84.0	2.3	0.68	385.2	0.11	0.72	0.87	6.66	1.33	5.92	—	—
17	-0.14 ± 0.02	−70.1	2.4	0.68	433.6	0.10	0.78	1.01	7.74	1.39	5.96	—	—
18	-0.13 ± 0.01	−78.4	2.6	0.68	375.9	0.10	0.76	0.91	9.14	1.29	6.72	—	—
19	-0.11 ± 0.01	−88.3	2.6	0.65	301.9	0.10	0.72	0.84	7.56	1.14	8.41	—	—
20	-0.10 ± 0.08	44.0	3.6	0.62	206.4	0.12	0.62	1.86	63.73	1.50	63.28	—	—
21	-0.08 ± 0.02	−135.9	2.9	0.76	307.1	0.09	0.84	0.76	4.39	0.94	6.03	—	—
22	-0.06 ± 0.01	−166.8	2.8	0.72	207.8	0.08	0.81	0.50	6.16	1.10	12.51	—	—
23	$-0.06 \pm < 0.01$	−178.0	2.5	0.66	147.9	0.08	0.73	0.39	6.26	1.25	13.73	—	—
24	0.26 ± 0.15	54.7	1.1	0.23	−23.5	0.06	0.27	0.19	5.47	1.34	8.62	0.40 ± 0.05	1.5
25	0.64 ± 0.32	17.6	1.1	0.18	−31.3	0.03	0.21	0.29	4.35	1.12	3.82	0.32 ± 0.05	2.0
26	0.78 ± 1.04	35.2	1.0	0.19	−20.9	0.05	0.24	0.21	5.79	1.32	5.80	0.20 ± 0.05	2.3
27	0.98 ± 0.81	19.7	0.9	0.14	−15.6	0.04	0.16	0.24	6.99	1.36	30.44	0.40 ± 0.05	1.5

TABLE 1. Main characteristics of the selected runs: the atmospheric stability parameter ζ, the Obukhov length L (m), the mean wind speed at canopy top U_h (m s^{-1}), the friction velocity u_* (m s^{-1}), the sensible heat flux (W m^{-2}), the turbulent intensity σ_u/U_c (where σ_u is the standard deviation of the longitudinal velocity and U_c the eddy convection velocity), the vertical velocity standard deviation σ_w (m s^{-1}), the air temperature standard deviation σ_θ (K), the integral time scale of the longitudinal velocity L_u (s), the integral time scale of the vertical velocity L_w (s), the integral time scale of the air temperature L_θ (s), the fractal dimension of the strong cliff singularities ($D(h=0)$) and the critical value of q at the phase transition (q_{crit}).

for the wavelet scale a; $\overline{\psi}$ denotes the complex conjugate of ψ. In our study, a third derivative of the Gaussian function was chosen as the wavelet (in which case the complex conjugate of ψ identifies to ψ). This wavelet is well localized in both space and frequency and is well suited to detecting discontinuities like cliffs in signals, as demonstrated by its extensive use with geophysical or medical signals (e.g. Muzy *et al.* 1994; Arneodo *et al.* 1995; Venugopal *et al.* 2006; Gerasimova *et al.* 2014; Attuel *et al.* 2018). More importantly, this wavelet allows us to remove polynomial trends of order less than or equal to three from the function $f(t)$, which is important when dealing with long meteorological time series.

The singularities of the signal f are then localized from the maximum lines of the wavelet transform modulus $|T_\psi[f](t, a)|$ of f, connected across scales a at time t as $a \to 0^+$. The strength of these singularities, also called local Hölder exponents

$h(t)$ (Mallat & Hwang 1992), are precisely the scaling exponents of the WTMM line pointing at the singularity. These lines define the wavelet transform skeleton $\mathcal{L}(a)$.

Under the canonical multifractal formalism, the distribution of h values given by the singularity spectrum $D(h)$ characterizes the set of singularities, and hence the fractal properties of the signal; $D(h)$ is computed through a Legendre transformation (2.2) of the scaling exponent $\tau(q)$ of the partition functions $Z(q, a)$ (2.3) restricted to the subset of points of the WTMM skeleton $\mathcal{L}(a)$ at each scale a

$$D(h) = \min_q [qh - \tau(q)], \tag{2.2}$$

$$Z(q, a) = \sum_{l \in \mathcal{L}(a)} \left[\sup_{(t,a') \in l, a' \leqslant a} |T_\psi[f](t, a')| \right]^q \sim a^{\tau(q)}, \tag{2.3}$$

where $q \in \mathbb{R}$ is the moment order. To avoid numerical instabilities inherent to the Legendre transform, the expectation values $h(q, a) = \partial[\ln(Z(q, a))]/\partial q$ and $D(q, a) = q\partial[\ln(Z(q, a))]/\partial q - \ln(Z(q, a))$ were computed first (Arneodo *et al.* 1995). Then, the slopes of $h(q, a)$ and $D(q, a)$ versus $\ln a$ gave $h(q)$ and $D(q)$, and therefore the $D(h)$ singularity spectrum as a curve parametrized by q.

The maximum moment order q chosen in our analysis was based on (i) the convergence of the moments of the wavelet coefficients along the time series for scales within the scaling regime, and (ii) the quality of the scaling of the partition function $\log_2(Z(q, a))$ versus the normalized scale $\log_2(a/L_w)$. Figure 1 shows an example of convergence with time of the moment of order 6 of the u and θ wavelet coefficients at two scales delimiting the scaling regime, for an unstable, near neutral and stable run. The convergence appears relatively well attained during the last 10 % of the time series, with variations lower than ± 10 % of the final value. This accuracy validation of the choice of the moment order is similar to the convergence method proposed by Anselmet *et al.* (1984). Analysing the scaling of the partition functions for moment order q up to 8 demonstrated that the range of scales for a valid estimation of the scaling exponent was drastically shortened for q larger than 6. The maximum moment order q was fixed to 6.

Finally, figures 2 to 4 illustrate the wavelet transform analysis of portions of the θ and u time series at the top of the canopy for an unstable, a near neutral and a stable case, runs 7, 19 and 27, respectively. Unlike the u signal, the θ signal exhibits ramp–cliff structures in non-neutral cases. In the unstable case, these structures correspond to gradual rise of air temperature with weak scalar fluctuations over scales commensurate with the integral scale, followed by a relatively sharp drop. As expected, in the stable case, these ramp–cliff patterns in the θ signal are inverted due to the inversion of the temperature vertical gradient. In the near-neutral case, the ramp–cliff structures are not as well defined for this transitional regime between uprising and decreasing ramps. The maximum lines of the wavelet transform modulus define the wavelet transform skeleton (figures 2–4*c*). The cliff singularities appear on the wavelet transform modulus as cone-like structures pointing toward the signal discontinuities or singularities at the smallest scales, while the ramp structures give a smaller and smoother wavelet transform modulus (weaker singularities) (figures 2–4*b*). The strongest cliff singularities visible on the non-neutral cases have the longest maximum lines, crossing all scales, with a slow decrease of the modulus $|T_\psi[\theta](t, a)|$ along their maximum lines as $a \to 0^+$, leading to near-zero Hölder exponents. Interestingly, the time-scale distributions of the wavelet transform modulus of both the θ and u signals show some branching structures, starting from large

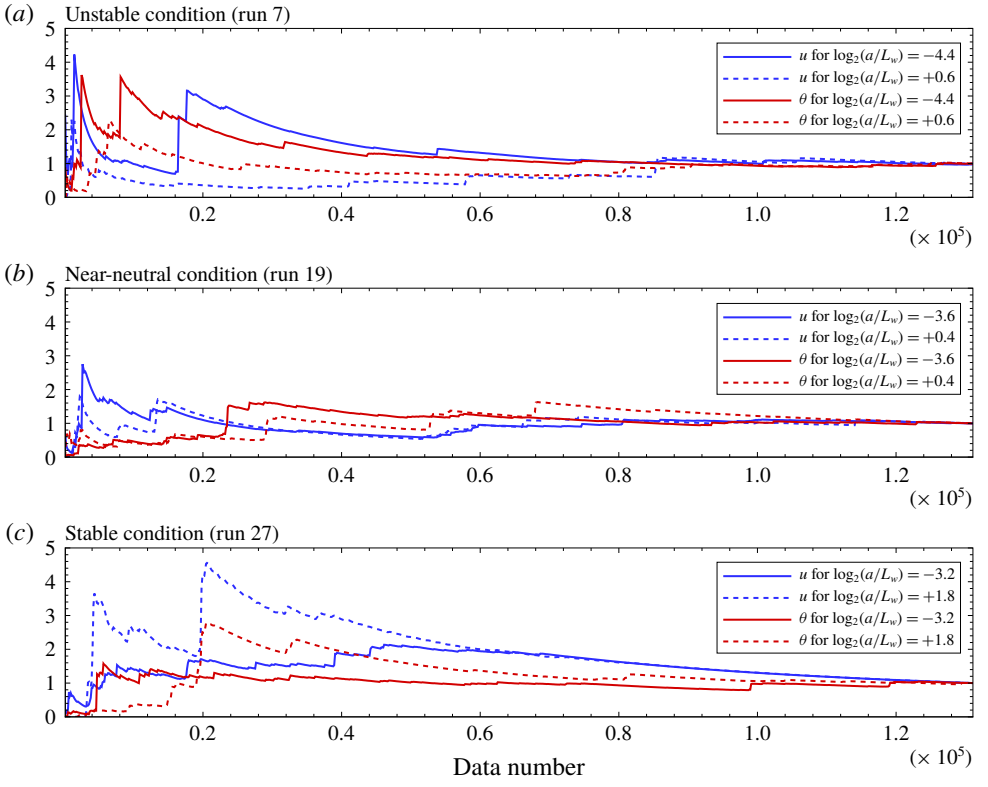

FIGURE 1. Convergence with time of the moment order 6 of the u and θ wavelet coefficients at two scales delimiting the scaling regime, for an unstable (a), near neutral (b) and stable (c) run.

scales where eddies divide asymmetrically into smaller ones, and so on, as depicted in figures 2(*b–e*) and 3(*b–e*) through the imbrication of cone-like structures related to abrupt changes in the signals at different scales. This hierarchical distribution of the wavelet transform modulus is similar to the branching structure obtained from a non-homogeneous Cantor set, resulting from deterministic hierarchical construction rules (see figure 1 in Argoul *et al.* (1989)). This represents a visual evidence that the singularities appear hierarchically distributed on a 'Cantor-like' set, suggesting the presence of a multiplicative cascading process, as previously reported by Argoul *et al.* (1989) from a velocity field of wind-tunnel turbulence at very high Reynolds numbers.

3. Results

3.1. *Multifractal characteristics of θ and u*

The WTMM analysis of the air temperature time series is illustrated in figure 5 for the unstable run 7. It reveals two scaling regimes over two successive ranges of scales within the inertial convective subrange ($a < L_\theta$), for $q = -0.5$ to 6 (figure 5*a–c*). This is visible from the log–log plot of the partition function $Z(q, a)$ as a function of the scale a. The first scaling regime occurs at scales smaller than L_w, while the second

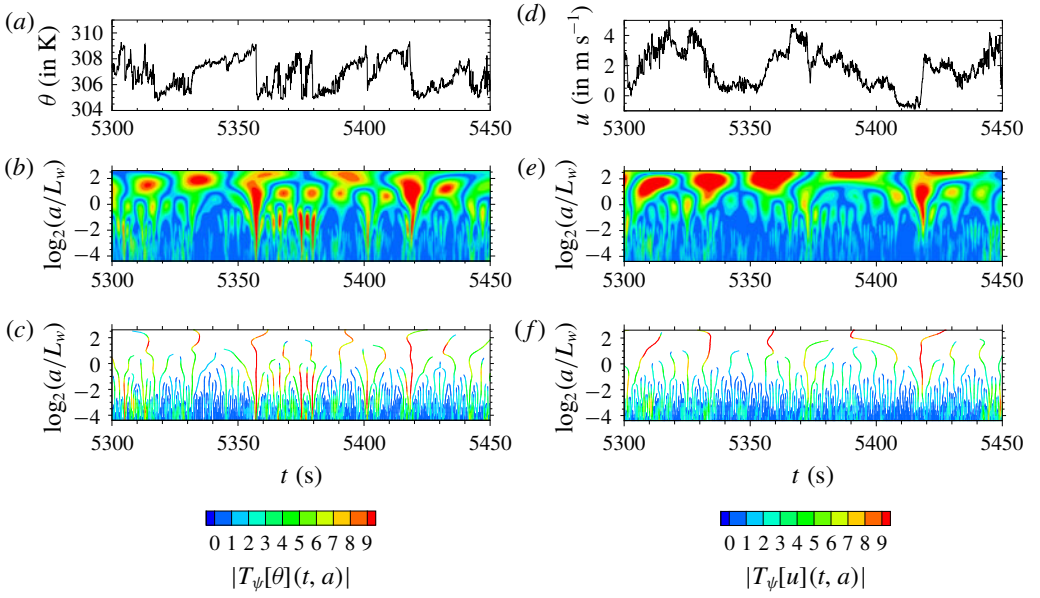

FIGURE 2. Wavelet transform analysis of an air temperature time series ($\theta(t)$) and a longitudinal wind velocity time series ($u(t)$) of length ~ 24 integral scales, measured at the canopy top in an unstable atmospheric regime (run 7 in table 1). (*a*,*d*) θ and u time series on a 150 s interval, the ramp–cliff patterns are visible in $\theta(t)$. (*b*,*e*) Moduli $|T_\psi[\theta](t, a)|$ and $|T_\psi[u](t, a)|$ of the wavelet transforms of $\theta(t)$ and $u(t)$, respectively. (*c*,*f*) Wavelet transform skeleton defined by the WTMM lines. The colour of the maximum lines corresponds to $|T_\psi|$. Panels (*b*,*c*,*e*,*f*) have the same colour map coding. The scale a is normalized by the integral scale of the vertical velocity (L_w).

scaling regime extends up to L_w. Hereafter, these regimes are referred to as scaling I and II.

The scaling exponent $\tau_I(q)$ obtained for the scaling regime I from the linear regression fit of $\log_2(Z(q, a))$ versus $\log_2(a)$, has a nonlinear convex increasing form. This form is well approximated by a quadratic spectrum $\tau_I(q) = -c_0^\theta + c_1^\theta q - c_2^\theta q^2/2!$ (figure 5*d*), where c_0^θ, c_1^θ, and c_2^θ are fitting coefficients (table 2). This spectrum $\tau_I(q)$ fits well with that obtained for temperature in homogeneous and isotropic flows of the Modane wind tunnel and other experiments (Schmitt 2005). The nonlinear form of $\tau_I(q)$ is corroborated by the dependence of the scaling behaviour of $h(q, a)$ versus q, suggesting a range of singularity exponents (h) in the signal. Hence, the singularity spectrum $D_I(h)$ exhibits a single humped shape over a finite range of Hölder exponents, varying from $h_{min} = 0.1$ to $h_{max} = 0.5$ for q decreasing from 6 to -0.5 (figure 5*e*). This represents the signature of the multifractality of the temporal fluctuations of $\theta(t)$.

The scaling regime II exhibits a saturation of $\tau_{II}(q)$ for high q values: $\tau_{sat} \sim -0.37$ (figure 5*d*). Interestingly, $\tau_{II}(q)$ and $D_{II}(h)$ spectra are similar to $\tau_I(q)$ and $D_I(h)$ spectra for low q values, respectively (figure 5*d–e*). Looking closer, the slopes of $\log_2(Z_{II}(q, a))$, $h_{II}(q, a)$ and $D_{II}(q, a)$ versus $\log_2(a/L_w)$ at low q values appear as the continuation of the slopes of the scaling regime I (figure 5*a–c*). Interestingly, the cross-over of $h(q, a)$ between the scaling regimes I and II evolves with q, the slope of $h(q, a)$ decreases from the larger scale of the scaling regime II, and invades

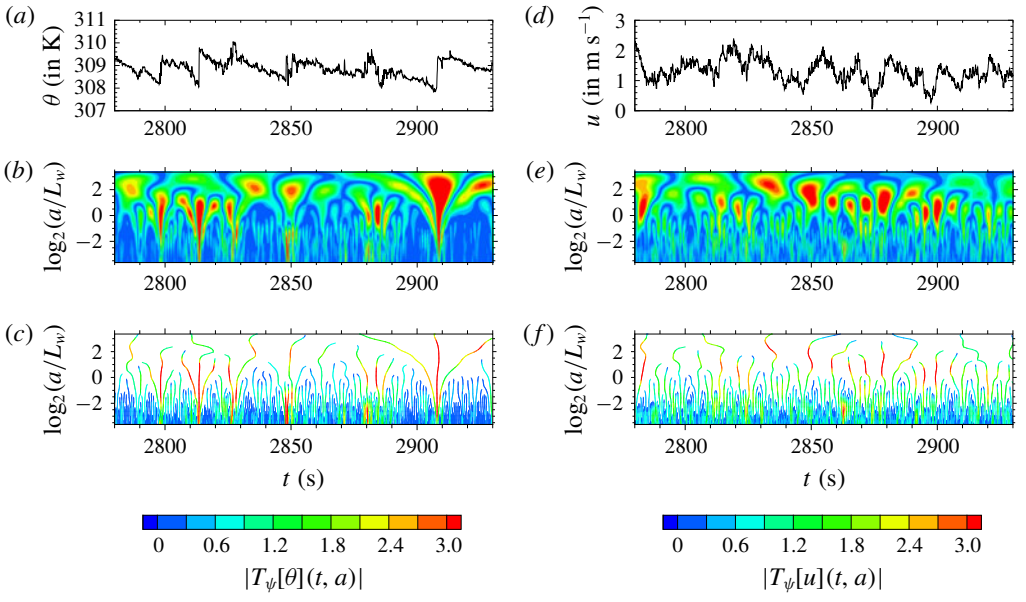

FIGURE 3. Same as figure 2 but for a stable atmospheric regime (run 27 in table 1). The air temperature time series ($\theta(t)$) is approximately 20 integral scales long.

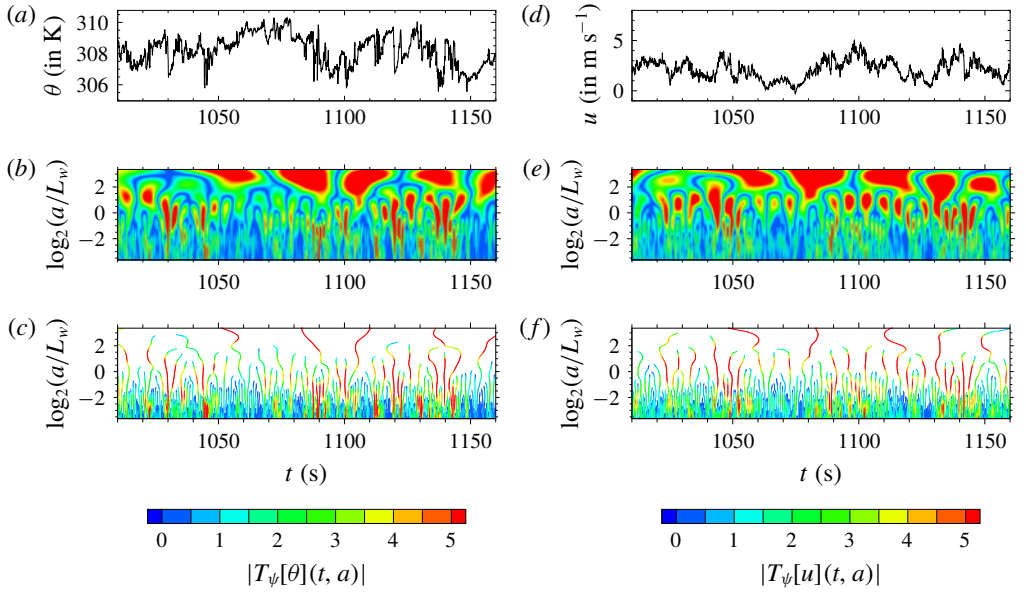

FIGURE 4. Same as figure 2 but for a near-neutral atmospheric regime (run 19 in table 1). The air temperature time series ($\theta(t)$) is approximately 49 integral scales long.

progressively the smaller scales with increasing q, reflecting the dominance of strong singularities ($h = 0$) for high q values (figure 5*b*). These strong singularities are the signature of the cliff patterns observed in figure 2. Concomitantly, $D_{II}(h)$ extends

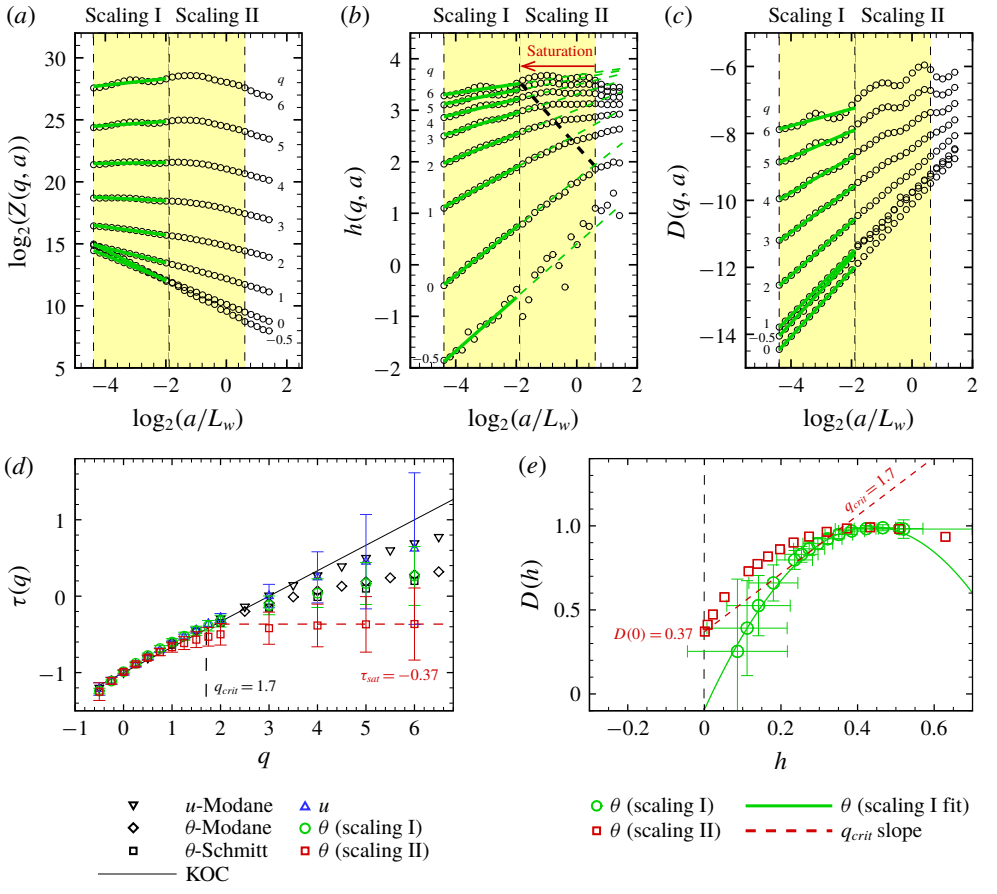

FIGURE 5. Multifractal analysis of the canopy-top air temperature under an unstable atmospheric regime (run 7 in table 1) using the WTMM method. (*a*) Partition function $\log_2(Z(q,a))$ versus $\log_2(a/L_w)$. (*b*) $\log_2(h(q,a))$ versus $\log_2(a/L_w)$. The black dashed line delimits the progressive invaded scaling regime II toward smaller scales with increasing q. (*c*) $\log_2(D(q,a))$ versus $\log_2(a/L_w)$. (*d*) The scaling functions $\tau(q)$ versus the moment order q estimated by linear regression fit of $\log_2(Z(q,a))$ versus $\log_2(a)$ for both scaling regions, and compared with $\tau(q)$ of the isotropic–homogeneous turbulent flows of Modane, compiled experiments (Schmitt 2005) and prediction from KOC turbulence theory. The scaling function $\tau(q)$ obtained for the longitudinal wind velocity (u) is also presented and compared with the Modane values. (*e*) The singularity spectra $D(h)$ versus the singularity strength h obtained from linear regression fits of $\log_2(h(q,a))$ and $\log_2(D(q,a))$ versus $\log_2(a)$. The red dashed line represents the linear extension of $D_{II}(h)$ fall off towards $+0.37$ for $h=0$ ($D_{II}(h=0) = -\tau_{sat}$) with a slope equal to q_{crit}. For clarity, error bars on $D(h)$ are partially represented. In (*a–c*), the two yellow boxes delimit the two scaling regimes I and II. The green solid lines represent the linear fit for the scaling regime I. The dashed green lines in (*b*) extend the linear fit obtained for the scaling regime I into the scaling regime II to highlight the saturation propagation due to 'cliff' singularities with decreasing scale and increasing q.

toward smaller h than $D_I(h)$ as the strong cliff singularities become statistically significant for this scale range.

Run	Longitudinal velocity			Air temperature		
	c_0^u	c_1^u	c_2^u	c_0^θ	c_1^θ	c_2^θ
1	$1.00 \pm < 0.01$	$0.38 \pm < 0.01$	$0.03 \pm < 0.01$	0.99 ± 0.01	0.48 ± 0.03	0.11 ± 0.02
2	$1.00 \pm < 0.01$	$0.40 \pm < 0.01$	$0.04 \pm < 0.01$	0.98 ± 0.01	0.45 ± 0.03	0.10 ± 0.02
3	$1.01 \pm < 0.01$	$0.34 \pm < 0.01$	$0.04 \pm < 0.01$	0.99 ± 0.01	0.46 ± 0.02	0.10 ± 0.01
4	$0.99 \pm < 0.01$	0.36 ± 0.01	0.03 ± 0.01	0.99 ± 0.01	0.43 ± 0.02	0.09 ± 0.01
5	$1.00 \pm < 0.01$	$0.43 \pm < 0.01$	$0.04 \pm < 0.01$	1.00 ± 0.01	0.46 ± 0.02	0.11 ± 0.01
6	$1.00 \pm < 0.01$	$0.40 \pm < 0.01$	$0.04 \pm < 0.01$	1.00 ± 0.01	0.43 ± 0.01	0.08 ± 0.01
7	$1.00 \pm < 0.01$	$0.41 \pm < 0.01$	$0.05 \pm < 0.01$	0.99 ± 0.01	0.44 ± 0.02	0.09 ± 0.01
8	$1.00 \pm < 0.01$	$0.40 \pm < 0.01$	$0.05 \pm < 0.01$	0.98 ± 0.01	0.45 ± 0.02	0.10 ± 0.01
9	$1.00 \pm < 0.01$	$0.42 \pm < 0.01$	$0.05 \pm < 0.01$	0.99 ± 0.01	0.44 ± 0.02	0.09 ± 0.01
10	$1.00 \pm < 0.01$	$0.43 \pm < 0.01$	$0.04 \pm < 0.01$	0.98 ± 0.02	0.43 ± 0.02	0.09 ± 0.01
11	$0.99 \pm < 0.01$	$0.40 \pm < 0.01$	$0.03 \pm < 0.01$	1.00 ± 0.01	0.42 ± 0.02	0.11 ± 0.02
12	$1.01 \pm < 0.01$	$0.41 \pm < 0.01$	$0.03 \pm < 0.01$	0.99 ± 0.01	0.43 ± 0.02	0.09 ± 0.01
13	$1.00 \pm < 0.01$	$0.43 \pm < 0.01$	$0.05 \pm < 0.01$	0.99 ± 0.01	0.40 ± 0.01	0.07 ± 0.01
14	$1.00 \pm < 0.01$	$0.43 \pm < 0.01$	$0.05 \pm < 0.01$	0.99 ± 0.01	0.43 ± 0.02	0.09 ± 0.01
15	$1.01 \pm < 0.01$	$0.39 \pm < 0.01$	$0.04 \pm < 0.01$	0.99 ± 0.01	0.39 ± 0.01	0.08 ± 0.01
16	$1.00 \pm < 0.01$	0.44 ± 0.01	$0.04 \pm < 0.01$	0.98 ± 0.01	0.41 ± 0.02	0.07 ± 0.01
17	$1.00 \pm < 0.01$	$0.43 \pm < 0.01$	$0.04 \pm < 0.01$	0.99 ± 0.01	0.43 ± 0.02	0.10 ± 0.01
18	$1.01 \pm < 0.01$	$0.42 \pm < 0.01$	$0.04 \pm < 0.01$	0.98 ± 0.01	0.42 ± 0.02	0.09 ± 0.01
19	$1.00 \pm < 0.01$	$0.41 \pm < 0.01$	$0.04 \pm < 0.01$	0.98 ± 0.01	0.40 ± 0.02	0.08 ± 0.01
20	$1.00 \pm < 0.01$	0.40 ± 0.01	$0.03 \pm < 0.01$	0.98 ± 0.01	0.39 ± 0.02	0.07 ± 0.01
21	$1.00 \pm < 0.01$	$0.41 \pm < 0.01$	$0.04 \pm < 0.01$	0.99 ± 0.01	0.41 ± 0.02	0.10 ± 0.01
22	$1.00 \pm < 0.01$	0.44 ± 0.01	$0.04 \pm < 0.01$	0.99 ± 0.01	0.41 ± 0.01	0.09 ± 0.01
23	$1.00 \pm < 0.01$	$0.43 \pm < 0.01$	$0.05 \pm < 0.01$	1.00 ± 0.01	0.43 ± 0.01	0.09 ± 0.01
24	$1.00 \pm < 0.01$	$0.38 \pm < 0.01$	$0.03 \pm < 0.01$	0.98 ± 0.01	0.44 ± 0.02	0.08 ± 0.01
25	$1.00 \pm < 0.01$	$0.39 \pm < 0.01$	$0.02 \pm < 0.01$	$0.98 \pm < 0.01$	0.44 ± 0.01	0.10 ± 0.01
26	$1.00 \pm < 0.01$	$0.37 \pm < 0.01$	$0.04 \pm < 0.01$	0.99 ± 0.01	0.44 ± 0.01	0.09 ± 0.01
27	$0.99 \pm < 0.01$	$0.36 \pm < 0.01$	$0.03 \pm < 0.01$	$0.98 \pm < 0.01$	0.46 ± 0.01	0.10 ± 0.01

TABLE 2. Coefficients c_0, c_1 and c_2 of the polynomial expansion of $\tau(q)$ ($\tau(q) = -c_0 + c_1 q - c_2 q^2/2!$) obtained from the WTMM multifractal analysis of the longitudinal velocity u and air temperature θ (scaling I), for the 27 selected runs (table 1).

Unlike θ, the WTMM analysis of u for run 7 reveals only one scaling regime covering the two scaling regimes I and II of θ (figure 6). The $\tau(q)$ spectrum of u fits well with that observed for u in the Modane wind-tunnel experiment, with no sign of saturation. Importantly, as in Modane and in Antonia *et al.* (1984), u fluctuations exhibit a lower intermittency coefficient ($c_2^u = 0.04 \pm < 0.01$ on average) than θ fluctuations ($c_2^\theta = 0.09 \pm 0.01$ on average) (table 2).

These behaviours of the multifractal spectra of θ and u fluctuations have been systematically observed in all our runs under unstable conditions ($\zeta \leqslant -0.15$). The same analyses performed only on the half-length of the signals exhibited the same behaviours, showing that the saturation of the $\tau(q)$ spectrum of θ is not an artefact of the finite length of the signals (result not shown). In stable conditions ($\zeta \geqslant 0.26$), similar behaviours were also observed although the ramp–cliff patterns in the θ signal were inverted (see figures 7 and 8 for the run 27). However, in near-neutral conditions, the temperature multifractal spectra exhibit only one scaling regime up to L_w, as for u, without sign of saturation of $\tau(q)$ (see figure 8 for run 19). The spectra $\tau(q)$ of θ and u are both in agreement with those obtained from the Modane wind-tunnel

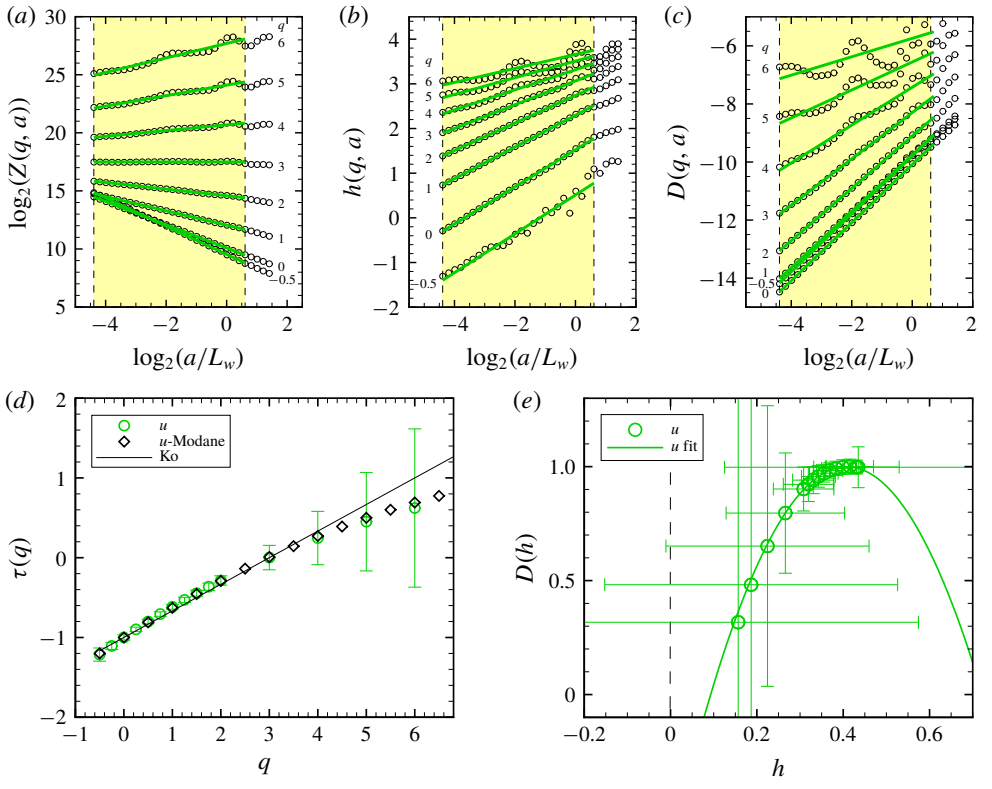

FIGURE 6. Multifractal analysis of the canopy-top longitudinal velocity under an unstable atmospheric regime (run 7 in table 1) using the WTMM method. (*a*) Partition function $\log_2(Z(q, a))$ versus $\log_2(a/L_w)$. (*b*) $\log_2(h(q, a))$ versus $\log_2(a/L_w)$. (*c*) $\log_2(D(q, a))$ versus $\log_2(a/L_w)$. (*d*) The scaling function $\tau(q)$ versus the moment order q estimated by linear regression fit of $\log_2(Z(q, a))$ versus $\log_2(a)$, and compared with $\tau(q)$ for the isotropic–homogeneous turbulent flows of Modane and prediction from Kolmogorov (Ko) turbulence theory. (*e*) The singularity spectrum $D(h)$ versus the singularity strength h obtained from linear regression fits of $\log_2(h(q, a))$ and $\log_2(D(q, a))$ versus $\log_2(a)$. In (*a–c*), the yellow box delimits the scaling regimes. The green solid lines represent the linear fit for the scaling regime.

experiment (figure 9*d*). Importantly, θ fluctuations are still more intermittent than u fluctuations (table 2).

Compared to θ and u, the scaling of the partition function of the vertical velocity component w was not as well defined at high-order moments. This is probably related to the much smaller integral scale of w (table 1). Consequently, the scaling functions $\tau(q)$ and the singularity spectra $D(h)$ obtained for w are compared with those from θ and u for only runs 12 (unstable condition), 17 (near-neutral condition) and 27 (stable condition), at small scales within the inertial convective subrange (figure 10). For larger scales, w fluctuations show no scaling regime due to their lower integral scale as compared to those of u and θ (table 1). Overall, at fine scales, $\tau(q)$ and $D(h)$ exhibit small differences between stability conditions. The scaling exponent $\tau(q)$ of w fluctuations appears lower than that of u fluctuations, which is consistent with observations from Katul, Porporato & Poggi (2009), and close to that of θ fluctuations,

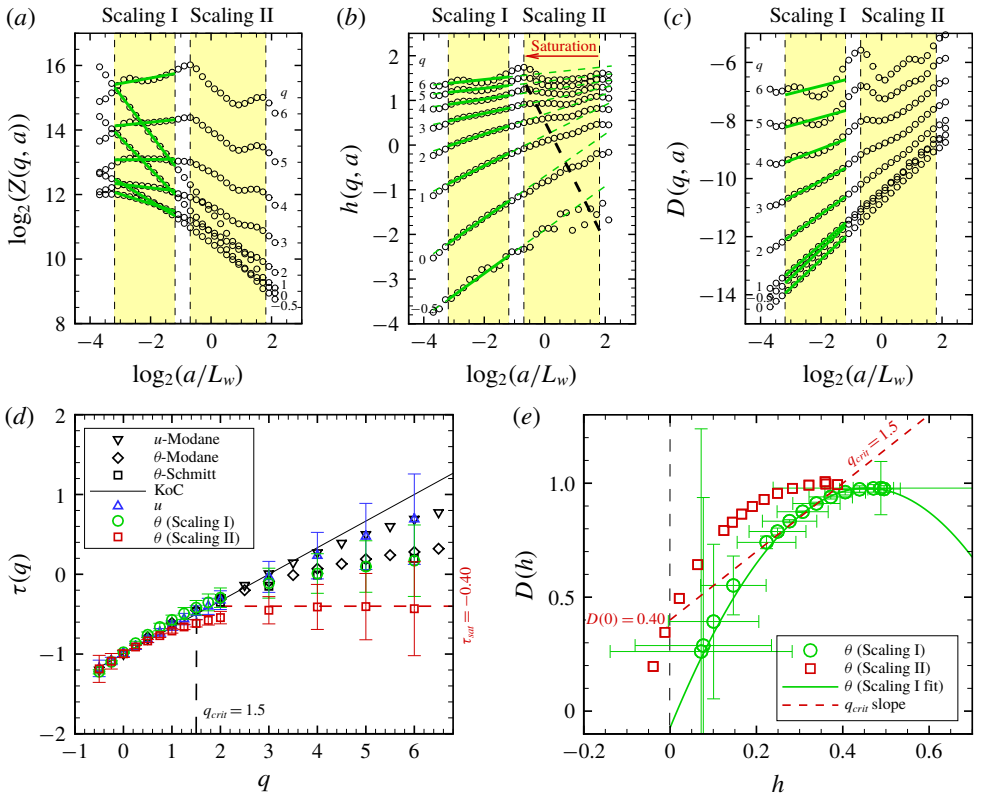

FIGURE 7. Same as figure 5 but for a stable atmospheric regime (run 27 in table 1).

although the intermittency of w (c_2 coefficient) is lower than the one of θ and slightly larger than the one of u. This is visible from the narrower singularity spectra $D(h)$ of w as compared to the singularity spectra of θ. The mean strength of the singularities of w (c_1 coefficient or the maximum of the singularity spectra) is stronger (lower c_1 coefficient) than the mean strength of θ singularities. This means that the fluctuations of w are on average sharper than those of θ, although the strongest fluctuations reach a similar strength in both signals ($h = 0$).

3.2. *Wavelet skewness and flatness factors of θ and u*

To confirm previous results on the larger intermittency of θ fluctuations than u fluctuations independently of the thermal stratification, the wavelet skewness factor (SF) and flatness factor (FF), i.e. skewness and flatness of the wavelet coefficients, of u and θ are presented in figure 11 for different stability regimes. Both factors were defined as follows:

$$\mathrm{SF}_f(a) = \langle T_\psi[f](t,a)'^3\rangle / \langle T_\psi[f](t,a)'^2\rangle^{3/2}, \tag{3.1}$$

and

$$\mathrm{FF}_f(a) = \langle T_\psi[f](t,a)'^4\rangle / \langle T_\psi[f](t,a)'^2\rangle^{4/2}, \tag{3.2}$$

where f is either u or θ, the brackets refer to time average and $T_\psi[f](t,a)' = T_\psi[f](t,a) - \langle T_\psi[f](t,a)\rangle$; $\langle T_\psi[f](t,a)'^2\rangle$ is the variance of the wavelet transform of f, $\langle T_\psi[f](t,a)'^3\rangle$ its moment of order 3 and $\langle T_\psi[f](t,a)'^4\rangle$ is its fourth-order moment.

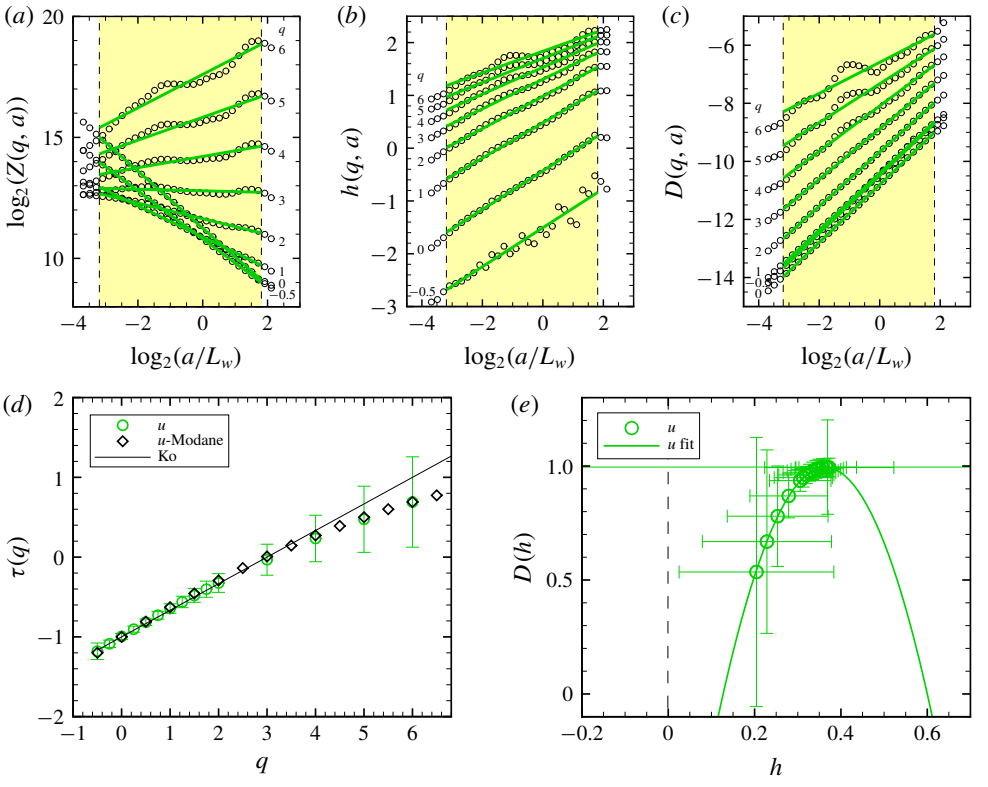

FIGURE 8. Same as figure 6 but for a stable atmospheric regime (run 27 in table 1).

Overall, u fluctuations appear in near-isotropic state with near-zero SF values, around -0.1 to -0.2, independently of the stability (figure 11*a*). This is consistent with the observed similarity at small scales ($a < L_w$) between the multifractal characteristics of u and those observed in homogeneous–isotropic turbulence (Modane, figure 5). The SF values of u obtained here for the mixing-layer-type flow prevailing at the canopy top are smaller than the values reported in atmospheric shear flows (Katul & Parlange 1994; Basu *et al.* 2007). The SF values of θ are larger in magnitude, with negative values (-0.5) in stable conditions and positive values ($+0.5$) in unstable conditions, reflecting the well-known anisotropic state of scalar turbulence at small scales (Sreenivasan 1991). The sign difference of SF_θ between unstable and stable conditions is consistent with previous observations (Katul & Parlange 1994, 1995), and was suspected to be related to the type of turbulence regime: isolated shear-overturning events in the stable condition and updraft–downdraft events in the unstable regime (Mahrt & Gamage 1987).

The flatness factors increase with decreasing scale, starting with Gaussian values ($+3$) near the integral scale (figure 11*b*). As expected, this increase is stronger for θ leading to larger FF values at smaller scales. This is consistent with the larger fine-scale intermittency of θ compared to u obtained from our multifractal analysis. This difference between FF_θ and FF_u is also in agreement with observations from Katul & Parlange (1994, 1995). Overall, the flatness factors appear weakly dependent on the stability. Only the θ flatness factors seem larger in stable conditions.

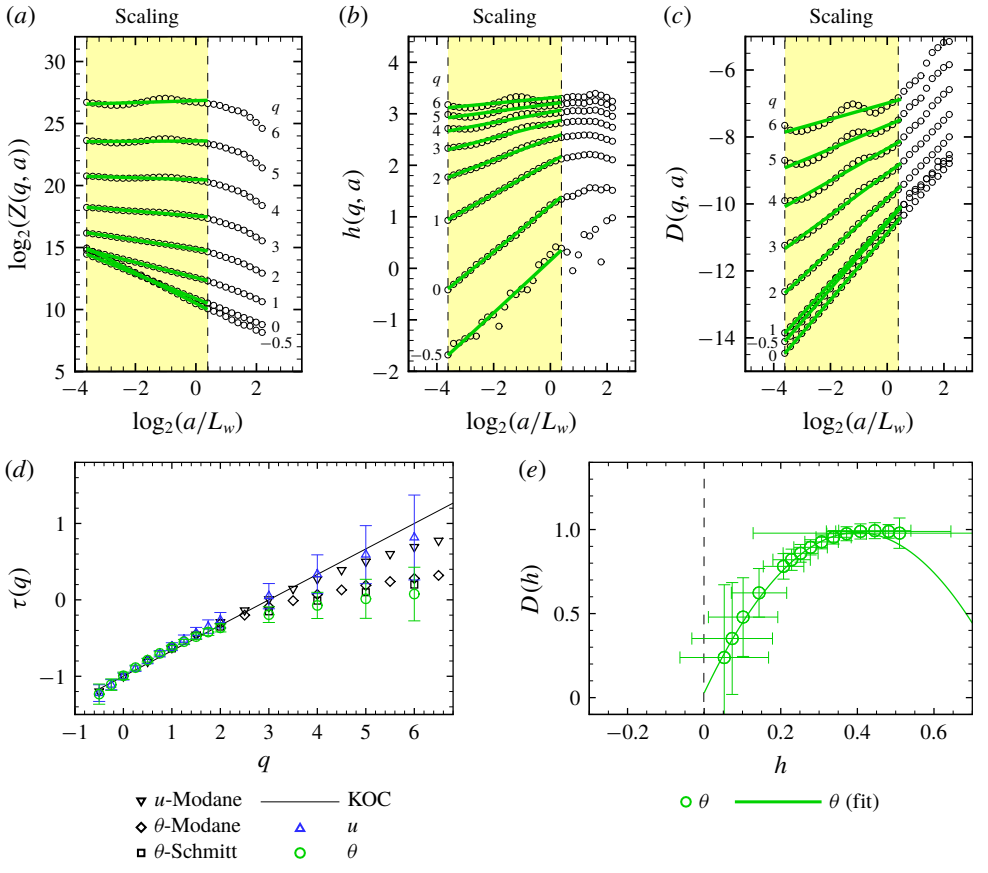

FIGURE 9. Same as figure 5 but under a near-neutral atmospheric regime (run 19 in table 1). Here, only one scaling regime is observed, covering the two scaling regimes I and II of the unstable convective regime of figure 5.

The small differences of SF and FF between non-neutral and near-neutral conditions do not permit us to distinguish an effect related to the presence or absence of saturation of the scaling exponent of θ observed in the previous section.

4. Discussion

Our multifractal analysis suggested a substantial similarity at small scales ($a < L_w/4$) between the multifractal characteristics of canopy-top u and θ fluctuations and those observed in homogenous–isotropic turbulence, for at least moment order q of up to 6. This was observed from the agreement of the scaling exponents $\tau(q)$ of u and θ in the scaling regime I with the well-known multifractal properties of isotropic–homogeneous turbulence (Arneodo *et al.* 1995; Schmitt 2005). This similarity is probably explained by the canopy-top mixing-layer-type flow weakening the anisotropy and inhomogeneity of the above atmospheric surface-layer shear flow. In near-neutral conditions, this similarity extends up to L_w. To our knowledge, this represents the first demonstration of the analogy between the fine-scale turbulence at the canopy top and that in an isotropic–homogeneous flow.

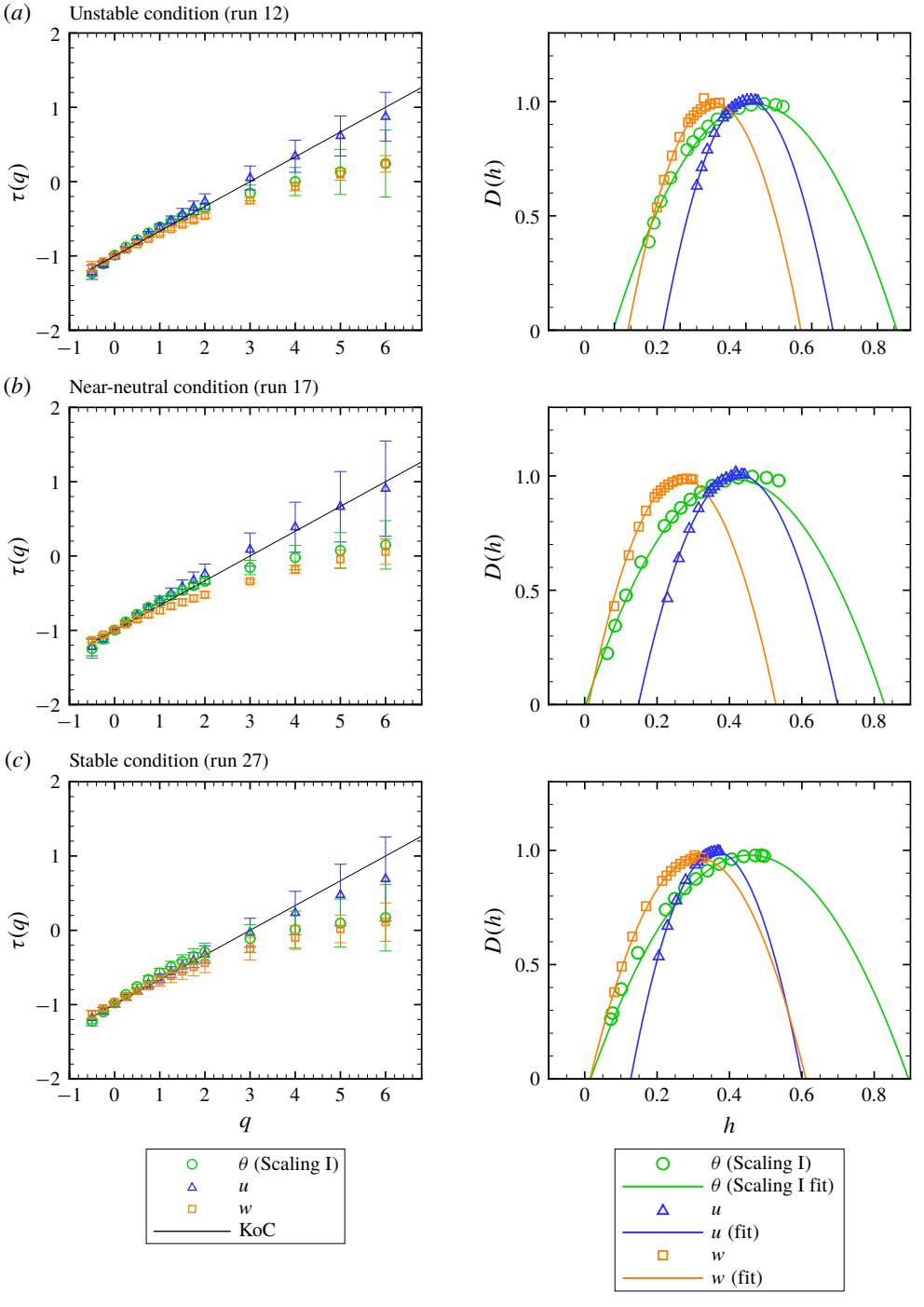

FIGURE 10. Comparison of the scaling functions $\tau(q)$ (left panels) and singularity spectra $D(h)$ (right panels) obtained for u, w and θ in the first scaling regime, for an unstable (a), near neutral (b) and stable (c) regime.

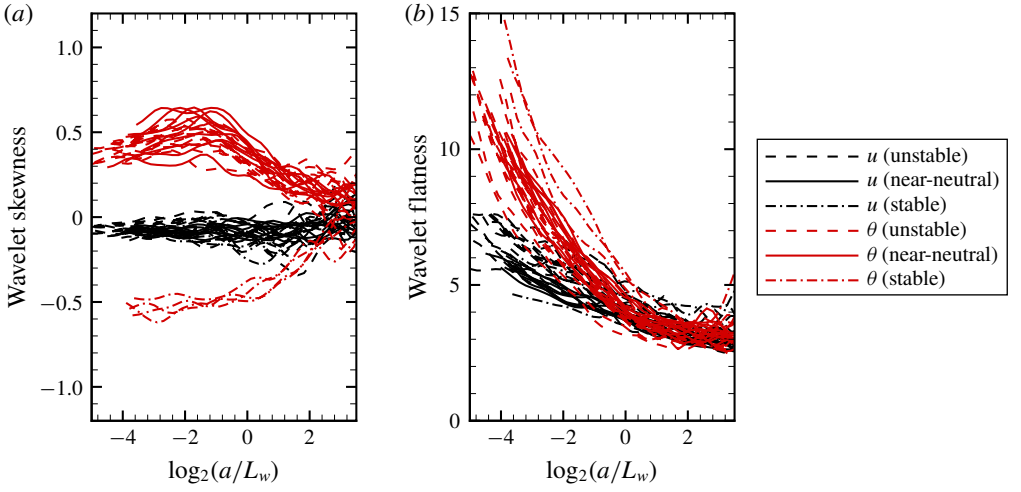

FIGURE 11. Wavelet skewness (a) and flatness (b) factors of u and θ, as a function of $\log_2(a/L_w)$ for the 27 runs, with distinction between unstable, near-neutral and stable conditions.

Under thermal stratification conditions (unstable or stable), steep cliffs (fronts) of large temperature gradients start to contaminate and saturate the multifractal spectra of θ fluctuations from high moment orders q, while the multifractal spectrum of u fluctuations remains similar to that in near-neutral conditions. This saturation due to cliff singularities was demonstrated for run 7 by the equivalence between the value of the scaling exponent at saturation ($\tau_{sat} = -0.37$ in figure 5d) and the value of the singularity spectrum for cliff singularities $D_{II}(h = 0) = 0.37$. This is further illustrated in figures 2(c) and 3(c) where cliffs dominate the WTMM lines for the scale range of the scaling regime II, while at smaller scales (regime I), the cliff singularities become embedded by numerous singularities of lower intensities. This saturation of the θ scaling exponent due to cliff structures was observed in all non-neutral runs and is consistent with previous modelling and laboratory measurements of scalar multifractal spectra (Celani *et al.* 2000; Moisy *et al.* 2001; Iyer *et al.* 2018).

We argue that this saturation of $\tau(q)$ in scaling regime II may reflect an ordered–disordered phase transition in signal singularities with decreasing moment order q. At high moment orders, strong cliff singularities dominate (ordered phase, $h = 0$) while at low moment orders, a large range of singularity strengths coexists (disordered phase, large range of h values). Such analogy between multifractal formalism and statistical thermodynamics has been demonstrated previously (Jensen, Kadanoff & Procaccia 1987; Katzen & Procaccia 1987; Arneodo *et al.* 1995), where q and $\tau(q)$ play the same role as the inverse temperature and the free energy. In particular, the non-analyticity of $\tau(q)$ has been interpreted as a phase transition occurring at a critical moment order q_{crit} (e.g. Barkley & Cumming 1990; Schertzer & Lovejoy 1992). Hence, this multifractal phase transition is analogous to a phase transition in condensed-matter physics, where systems show regular orientation of atoms with long-range correlation under the low-temperature phase and a random orientation of atoms with no long-range correlation under the high-temperature phase.

To verify this analogy between the saturation of $\tau(q)$ and a phase transition, we use the same approach as Arneodo *et al.* (1995). We assume that θ in scaling regime

II is the superposition of two signals, one with the multifractal characteristics of the scaling regime I and the other one corresponding to large-scale ramp–cliff patterns. The partition function of this signal can be then split into two parts: $Z_{II}(q, a) = Z_I(q, a) + Z_{cliff}(q, a) \sim a^{\tau_I(q)} + a^{\tau_{sat}}$, where Z_I and Z_{cliff} are the sum of partition functions over the maximum lines created by the first and second signals, corresponding to the scaling laws $a^{\tau_I(q)}$ and $a^{\tau_{sat}}$, respectively, in the limit $a \to 0^+$. In such conditions, a q critical value should exist such that

$$\tau_{II}(q) = \begin{cases} \tau_I(q), & q < q_{crit} \\ \tau_{sat}, & q \geqslant q_{crit}. \end{cases} \tag{4.1}$$

At the critical point, $\tau_{sat} = \tau_I(q_{crit}) \approx -c_0^\theta + c_1^\theta q_{crit} - c_2^\theta q_{crit}^2/2!$, which leads to

$$q_{crit} = \frac{c_1^\theta}{c_2^\theta} - \sqrt{\left(\frac{c_1^\theta}{c_2^\theta}\right)^2 + \frac{2}{c_2^\theta}(-\tau_{sat} - c_0^\theta)}. \tag{4.2}$$

For the temperature time series of figure 5, we obtained $q_{crit} = 1.7$. The saturation of $\tau_{II}(q)$ near -0.37 for $q \geqslant q_{crit}$ is in excellent agreement with the $D_{II}(h)$ fall off towards $+0.37$ for $h = 0$ ($D_{II}(h = 0) = -\tau_{sat}$). Furthermore, the linear extension of this fall off is tangent to the $D_I(h)$ spectrum with a slope equal to q_{crit} (figure 5*e*). This last feature is the signature of a phase transition phenomenon. The change of slope of $\tau_{II}(q)$ around q_{crit} suggests a first-order phase transition, but this cannot be concluded with certainty. Indeed, the $D_{II}(h)$ fall off is not perfectly linear for q values surrounding q_{crit}, and the non-analyticity of $\tau_{II}(q)$ is not perfect around q_{crit}. This is due to the shifting of the cross-over with q between regime I and the saturation regime, weakening the scaling regime II in this transition region (see $h(q, a)$ for q around 2 and 3 in figure 5*b*).

For unstable and stable conditions, q_{crit} ranges between 1.4 and 3.7 and the fractal dimension of the stronger cliffs ($h = 0$) varies from $D(h = 0) = 0.0$ to 0.40. Both q_{crit} and $D(h = 0)$ do not show a clear trend according to the stability intensity ζ (see table 1), which could be due to the varying large-scale meteorological conditions, even for similar stability levels. However, all runs in these stability conditions exhibited a saturation of $\tau(q)$ and the conditions of a phase transition, which demonstrates the robustness of our results.

One striking result from our multifractal analysis is the absence of saturation in the temperature multifractal spectra under near-neutral conditions. This was observed for the 9 near-neutral runs (table 1). This suggests a negligible impact of cliff singularities ($h = 0$) on the statistics of the θ signal. However, θ fluctuations still appear more intermittent than u fluctuations (see the c_2^θ and c_2^u coefficients in table 2), with the same level of intermittency in both unstable and stable conditions. This larger intermittency of θ fluctuations compared to u ones, independently of the stability conditions, was further confirmed by the larger increase of the θ wavelet flatness factor than the u one with decreasing scale (figure 11). This result is a strong indication that the statistical contribution of the 'cliffs' is not important enough ($D(h = 0) = 0$) to account for the stronger intermittency of θ fluctuations when compared to corresponding u fluctuations. This is also confirmed by the poor correlation of the fine-scale θ wavelet coefficients with the near-integral-scale ones, as illustrated in figure 12 for runs 7, 19 and 27 (unstable, near-neutral and stable cases). We suspect that the progressively invaded influence of the strongest singularities (cliffs) with increasing moment order q, from large to small scales, might lead to the saturation as well of the scalar scaling exponent at small scales (scaling regime I) for

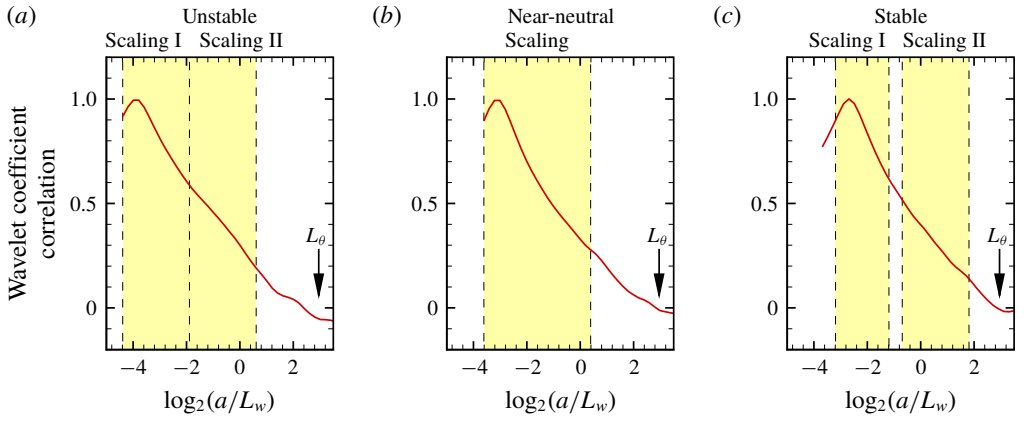

FIGURE 12. Correlation between the fine-scale modulus of the temperature wavelet transform (within the first scaling regime) and the equivalent larger-scale modulus for an unstable (run 7), near-neutral (run 19) and stable (run 27) regimes. The yellow boxes delimit the scaling regimes. The black arrows indicate the position of the integral scale. This figure confirms for all stability conditions the negligible correlation between $|T_\psi[\theta]|$ within the scaling regime I and $|T_\psi[\theta]|$ near the integral scale of θ fluctuations (L_θ). This means that fine-scale θ fluctuations are weakly impacted by large-scale ramp–cliff structures.

q values larger than the maximum q value considered in this study ($q = 6$), however, these rare and extreme singularities should be statistically insignificant and could not explain the larger intermittency of scalar fluctuations.

This statistically limited contribution of cliff structures to the intermittency of scalar fluctuations contrasts with the Zorzetto *et al.* (2018) findings on the persistence of the signature of integral-scale ramp–cliff structures on θ fluctuations, well within the inertial convective subrange, explaining the larger intermittency of θ fluctuations. We suspect that the mixing-layer-type flow prevailing at the top of our canopy dampens the memory of the integral-scale eddy structures as opposed to shear-layer flow located far above surface roughness elements of Zorzetto *et al.* (2018).

Our findings suggest that the scalar intermittency at fine scales has more of an internal origin, built from the fluctuation dissipation rate, than an external one, coming from large-scale external forcing (cliffs). Interestingly, the values of the intermittency coefficients c_2^θ (0.09 ± 0.01 on average) are close to those observed for Lagrangian velocity fluctuations in turbulent flows (0.08 ± 0.01 (Chevillard *et al.* 2003)). Hence, the dynamic of scalar fluctuations appear closer to the dynamic of Lagrangian velocity fluctuations than to that of Eulerian velocity fluctuations. This might be considered for explaining the larger intermittency of scalar fluctuations.

5. Summary

Under unstable and stable conditions, i.e. daily warming and nocturnal cooling conditions, our analysis revealed a saturation of the scaling exponent of the canopy-top air temperature (θ) fluctuations above a critical moment order, unlike that of the longitudinal wind velocity (u) fluctuations. This saturation is related to the sharp temperature fronts bordering the ramp–cliff patterns present in the θ signal. This suggests an ordered–disordered phase transition occurring at this critical moment

order. Under near-neutral conditions, no such phase transition was observed while θ fluctuations are still more intermittent at fine scales than u fluctuations. Hence, conversely to previous studies that suggested large-scale ramp–cliff structures as responsible for the larger intermittency of scalar turbulence at fine scales than that of velocity fluctuations, our multifractal analysis applied to canopy-top mixing-layer-type flow shows that the statistical contribution of the 'cliffs' is not significant enough to explain the stronger intermittency of θ fluctuations. Our findings open a new avenue on scalar turbulence intermittency, with an analogy to a phase transition of the invaded influence of the strongest singularities (cliffs) with increasing moment order, from large to small scales.

Acknowledgements

We would like to thank (i) E. Lamaud, J.-M. Bonnefond and D. Garrigou for their contribution to the field data collection, and (ii) C. Chipeaux and D. Loustau for their help with our experiment set-up at the Salles ICOS station. Financial support from the Department 'Environnement et Agronomie' of INRA is gratefully acknowledged. Finally, we thank the three anonymous reviewers for their helpful comments.

Declaration of interests

The authors report no conflict of interest.

REFERENCES

ABRY, P., ROUX, S. & JAFFARD, S. 2011 Detecting oscillating singularities in multifractal analysis: application to hydrodynamic turbulence. In *IEEE International Conference on Acoustics, Speech, and Signal Processing (ICASSP)*, pp. 4328–4331. Prague Congress Ctr, Prague, CZECH REPUBLIC.

ANSELMET, F., GAGNE, Y., HOPFINGER, E. J. & ANTONIA, R. A. 1984 High-order velocity structure functions in turbulent shear flows. *J. Fluid Mech.* **140**, 63–89.

ANTONIA, R. A., HOPFINGER, E. J., GAGNE, Y. & ANSELMET, F. 1984 Temperature structure functions in turbulent shear flows. *Phys. Rev.* A **30** (5), 2704–2707.

ARGOUL, F., ARNEODO, A., GRASSEAU, G., GAGNE, Y., HOPFINGER, E. J. & FRISCH, U. 1989 Wavelet analysis of turbulence reveals the multifractal nature of the Richardson cascade. *Nature* **338**, 51–53.

ARNEODO, A., AUDIT, B., DECOSTER, N., MUZY, J. F. & VAILLANT, C. 2002 A wavelet based multifractal formalism: application to DNA sequences, satellite images of the cloud structure and stock market data. In *The Science of Disasters: Climate Disruptions, Heart Attacks, and Market Crashes*, pp. 26–102. Springer.

ARNEODO, A., AUDIT, B., KESTENER, P. & ROUX, S. G. 2008 Wavelet-based multifractal analysis. *Scholarpedia* **3**, 4103.

ARNEODO, A., BACRY, E. & MUZY, J. F. 1995 The thermodynamics of fractals revisited with wavelets. *Physica* A **213**, 232–275.

ARNEODO, A., DECOSTER, N., KESTENER, P. & ROUX, S. G. 2003 A wavelet-based method for multifractal image analysis: from theoretical concepts to experimental applications. *Adv. Imaging Electr. Phys.* **126**, 1–92.

ARNEODO, A., MANNEVILLE, S. & MUZY, J. F. 1998*c* Towards log-normal statistics in high Reynolds number turbulence. *Eur. Phys. J.* B **1**, 129–140.

ARNEODO, A., MUZY, J. F. & SORNETTE, D. 1998*d* 'Direct' causal cascade in the stock market. *Eur. Phys. J.* B **2**, 277–282.

ARNEODO, A., VAILLANT, C., AUDIT, B., ARGOUL, F., D'AUBENTON CARAFA, Y. & THERMES, C. 2011 Multi-scale coding of genomic information: from dna sequence to genome structure and function. *Phys. Rep.* **498**, 45–188.

ATTUEL, G., GERASIMOVA-CHECHKINA, E., ARGOUL, F., YAHIA, H. & ARNEODO, A. 2018 Multifractal desynchronization of the cardiac excitable cell network during atrial fibrillation. I. Multifractal analysis of clinic data. *Front. Physiol.* **8**, 1139.

AUDIT, B., BACRY, E., MUZY, J. F. & ARNEODO, A. 2002 Wavelet-based estimators of scaling behavior. *IEEE Trans. Inf. Theory* **48**, 2938–2954.

BALKOVSKY, E. & LEBEDEV, V. 1998 Instanton for the Kraichnan passive scalar problem. *Phys. Rev.* E **58** (5, A), 5776–5795.

BARKLEY, D. & CUMMING, A. 1990 Thermodynamics of the quasiperiodic parameter set at the borderline of chaos: experimental results. *Phys. Rev. Lett.* **64** (4), 327–331.

BASU, S., FOUFOULA-GEORGIOU, E., LASHERMES, B. & ARNÉODO, A. 2007 Estimating intermittency exponent in neutrally stratified atmospheric surface layer flows: a robust framework based on magnitude cumulant and surrogate analyses. *Phys. Fluids* **19**, 115102.

BELCHER, S. E., HARMAN, I. N. & FINNIGAN, J. J. 2012 The wind in the willows: flows in forest canopies in complex terrain. *Annu. Rev. Fluid Mech.* **44**, 479–504.

CAVA, D. & KATUL, G. G. 2008 Spectral short-circuiting and wake production within the canopy trunk space of an alpine hardwood forest. *Boundary-Layer Meteorol.* **126**, 415–431.

CELANI, A., LANOTTE, A., MAZZINO, A. & VERGASSOLA, M. 2000 Universality and saturation of intermittency in passive scalar turbulence. *Phys. Rev. Lett.* **84** (11), 2385–2388.

CELANI, A., MAZZINO, A. & VERGASSOLA, M. 2001 Thermal plume turbulence. *Phys. Fluids* **13** (7), 2133–2135.

CHERTKOV, M. 1997 Instanton for random advection. *Phys. Rev.* E **55** (3, A), 2722–2735.

CHEVILLARD, L., ROUX, S. G., LEVEQUE, E., MORDANT, N., PINTON, J. F. & ARNEODO, A. 2003 Lagrangian velocity statistics in turbulent flows: effects of dissipation. *Phys. Rev. Lett.* **91** (21), 214502.

CORRSIN, S. 1951 On the spectrum of isotropic temperature fluctuations in an isotropic turbulence. *J. Appl. Phys.* **22** (4), 469–473.

DELOUR, J., MUZY, J. F. & ARNEODO, A. 2001 Intermittency of 1d velocity spatial profiles in turbulence: a magnitude cumulant analysis. *Eur. Phys. J.* B **23**, 243–248.

DUPONT, S., IRVINE, M. R., BONNEFOND, J. M., LAMAUD, E. & BRUNET, Y. 2012 Turbulent structures in a pine forest with a deep and sparse trunk space: stand and edge regions. *Boundary-Layer Meteorol.* **143**, 309–336.

DUPONT, S. & PATTON, E. G. 2012 Momentum and scalar transport within a vegetation canopy following atmospheric stability and seasonal canopy changes: the CHATS experiment. *Atmos. Chem. Phys.* **12**, 5913–5935.

FALKOVICH, G., GAWEDZKI, K. & VERGASSOLA, M. 2001 Particles and fields in fluid turbulence. *Rev. Mod. Phys.* **73** (4), 913–975.

FINNIGAN, J. 2000 Turbulence in plant canopies. *Annu. Rev. Fluid Mech.* **32**, 519–571.

FITZMAURICE, L., SHAW, R. H., PAW U, K. T. & PATTON, E. G. 2004 Three-dimensional scalar microfront systems in a large-eddy simulation of vegetation canopy flow. *Boundary-Layer Meteorol.* **112**, 107–127.

FRISCH, U. 1995 *Turbulence*, p. 296. Cambridge University Press.

FRISCH, U., MAZZINO, A. & VERGASSOLA, M. 1998 Intermittency in passive scalar advection. *Phys. Rev. Lett.* **80** (25), 5532–5535.

GAO, W., SHAW, R. H. & PAW U, K. T. 1989 Observation of organised structures in turbulent flow within and above a forest canopy. *Boundary-Layer Meteorol.* **47**, 349–377.

GERASIMOVA, E., AUDIT, B., ROUX, S. G., KHALIL, A., GILEVA, O., ARGOUL, F., NAIMARK, O. & ARNEODO, A. 2014 Wavelet-based multifractal analysis of dynamic infrared thermograms to assist in early breast cancer diagnosis. *Front. Physiol.* **5**, 176.

HARMAN, I. N. & FINNIGAN, J. J. 2008 Scalar concentration profiles in the canopy and roughness sublayer. *Boundary-Layer Meteorol.* **129**, 323–351.

HIGBIE, R. 1935 The rate of absorption of a pure gas into a still liquid during short periods of exposure. *Trans. Am. Inst. Chem. Engng* **31**, 365–389.

HIGGINS, C. W., PARLANGE, M. B. & MENEVEAU, C. 2003 Alignment trends of velocity gradients and subgrid-scale fluxes in the turbulent atmospheric boundary layer. *Bound. Layer Meteorol.* **109** (1), 59–83.

IYER, K. P., SCHUMACHER, J., SREENIVASAN, K. R. & YEUNG, P. K. 2018 Steep cliffs and saturated exponents in three-dimensional scalar turbulence. *Phys. Rev. Lett.* **121** (26), 264501.

JENSEN, M. H., KADANOFF, L. P. & PROCACCIA, I. 1987 Scaling structure and thermodynamics of strange sets. *Phys. Rev.* A **36** (3), 1409–1420.

KAIMAL, J. C. & FINNIGAN, J. J. 1994 *Atmospheric Boundary Layer Flows. Their Structure and Measurements*, p. 289. Oxford University Press.

KATUL, G. G. & CHANG, W. H. 1999 Principal length scales in second-order closure models for canopy turbulence. *J. Appl. Meteorol.* **38**, 1631–1643.

KATUL, G. G., ANGELINI, C., DE CANDITIIS, D., AMATO, U., VIDAKOVIC, B. & ALBERSTON, J. D. 2003 Are the effects of large scale flow conditions really lost through the turbulent cascade? *Geophys. Res. Lett.* **30** (4), 1164.

KATUL, G. G., CAVAC, D., SIQUERIA, M. & POGGI, D. 2013 Scalar turbulence within the canopy sublayer. In *Coherent Flow Structures at Earth's Surface*, pp. 73–95. John Wiley.

KATUL, G. G. & PARLANGE, M. B. 1994 On the active role of temperature in surface-layer turbulence. *J. Atmos. Sci.* **51** (15), 2181–2195.

KATUL, G. G. & PARLANGE, M. B. 1995 The spatial structure of turbulence at production wavenumbers using orthonormal wavelets. *Boundary-Layer Meteorol.* **75**, 81–108.

KATUL, G. G., PORPORATO, A., CAVA, D. & SIQUEIRA, M. 2006 An analysis of intermittency, scaling, and surface renewal in atmospheric surface layer turbulence. *Physica* D **215**, 117–126.

KATUL, G. G., PORPORATO, A. & POGGI, D. 2009 Roughness effects on fine-scale anisotropy and anomalous scaling in atmospheric flows. *Phys. Fluids* **21**, 035106.

KATZEN, D. & PROCACCIA, I. 1987 Phase transitions in the thermodynamic formalism of multifractals. *Phys. Rev. Lett.* **58** (12), 1169–1172.

KHALIL, A., JONCAS, G., NEKKA, F., KESTENER, P. & ARNEODO, A. 2006 Morphological analysis of hi features. II. Wavelet-based multifractal formalism. *Astrophys. J. Suppl. Ser.* **165**, 512–550.

KOLMOGOROV, A. N. 1941 Local structure of turbulence in an incompressible fluid for very large reynolds numbers. *Dokl. Akad. Nauk. SSSR* **30**, 299–303.

LASHERMES, B., ROUX, S., ABRY, P. & JAFFARD, S. 2008 Comprehensive multifractal analysis of turbulent velocity using the wavelet leaders. *Eur. Phys. J.* B **61**, 201–215.

LIN, C. C. 1953 On Taylor's hypothesis and the acceleration terms in the Navier–Stokes equations. *Q. Appl. Maths* **10** (4), 154–165.

LVOV, V. S., PROCACCIA, I. & FAIRHALL, A. L. 1994 Anomalous scaling in fluid-mechanics – the case of the passive scalar. *Phys. Rev.* E **50** (6), 4684–4704.

MAHRT, L. & GAMAGE, N. 1987 Observation of turbulence in stratified flow. *J. Atmos. Sci.* **44** (7), 1106–1121.

MALLAT, S. & HWANG, W. L. 1992 Singularity detection and processing with wavelets. *IEEE Trans. Inf. Theory* **38** (2, 2), 617–643.

MENEVEAU, C., LUND, T. S. & CABOT, W. H. 1996 A Lagrangian dynamic subgrid-scale model of turbulence. *J. Fluid Mech.* **319**, 353–385.

MOISY, F., WILLAIME, H., ANDERSEN, J. S. & TABELING, P. 2001 Passive scalar intermittency in low temperature helium flows. *Phys. Rev. Lett.* **86** (21), 4827–4830.

MUZY, J. F., BACRY, E. & ARNEODO, A. 1991 Wavelets and multifractal formalism for singular signals: application to turbulence data. *Phys. Rev. Lett.* **67**, 3515–3518.

MUZY, J. F., BACRY, E. & ARNEODO, A. 1993 Multifractal formalism for fractal signals – the structure-function approach versus the wavelet-transform modulus-maxima method. *Phys. Rev.* E **47** (2), 875.

MUZY, J. F., BACRY, E. & ARNEODO, A. 1994 The multifractal formalism revisited with wavelets. *Int. J. Bifurc. Chaos* **4**, 245–302.

OBUKHOV, A. 1949 Structure of the temperature field in a turbulent current. *Tr. Inst. Teor. Geofiz. Akad. Nauk. SSSR.* **13** (1), 58–69.

OBUKHOV, A. M. 1946 Turbulence in an atmosphere with a non-uniform temperature. *Tr. Inst. Teor. Geofiz. Akad. Nauk. SSSR.* **1**, 95–115.

PAW U, K. T., BRUNET, Y., COLLINEAU, S., SHAW, R. H., MAITANI, T., QIU, J. & HIPPS, L. 1992 On coherent structures in turbulence above and within agricultural plant canopies. *Agric. Forest Meteorol.* **61**, 55–68.

PAW U, K. T., QIU, J., SU, H.-B., WATANABE, T. & BRUNET, B. 1995 Surface renewal analysis: a new method to obtain scalar fluxes. *Agric. Forest Meteorol.* **74**, 119–137.

POGGI, D., PORPORATO, A., RIDOLFI, L., ALBERTSON, J. D. & KATUL, G. G. 2004 The effect of vegetation density on canopy sub-layer turbulence. *Boundary-Layer Meteorol.* **111** (3), 565–587.

POPE, S. 2000 *Turbulent Flows*. Cambridge University Press.

PUMIR, A., SHRAIMAN, B. I. & SIGGIA, E. D. 1997 Perturbation theory for the delta-correlated model of passive scalar advection near the Batchelor limit. *Phys. Rev.* E **55** (2), R1263–R1266.

RAUPACH, M. R., FINNIGAN, J. J. & BRUNET, Y. 1996 Coherent eddies and turbulence in vegetation canopies: the mixing-layer analogy. *Boundary-Layer Meteorol.* **78** (3–4), 351–382.

ROLAND, T., KHALIL, A., TANENBAUM, A., BERGUIGA, L., DELICHERE, P., BONNEVIOT, L., ELEZGARAY, J., ARNEODO, A. & ARGOUL, F. 2009 Revisiting the physical processes of vapodeposited thin gold films on chemically modified glass by atomic force and surface plasmon microscopies. *Surf. Sci.* **603** (22), 3307–3320.

ROUX, S. G., VENUGOPAL, V., FIENBERG, K., ARNEODO, A. & FOUFOULA-GEORGIOU, E. 2009 Evidence for inherent nonlinearity in temporal rainfall. *Adv. Water Resour.* **32**, 41–48.

SCHERTZER, D. & LOVEJOY, S. 1992 Hard and soft multifractal processes. *Physica* A **185**, 187–194.

SCHMITT, F. G. 2005 Relating lagrangian passive scalar scaling exponents to Eulerian scaling exponents in turbulence. *Eur. Phys. J.* B **48**, 129–137.

SCHMITT, F., SCHERTZER, D., LOVEJOY, S. & BRUNET, Y. 1996 Multifractal temperature and flux of temperature variance in fully developed turbulence. *Europhys. Lett.* **34** (3), 195–200.

SHRAIMAN, B. I. & SIGGIA, E. D. 2000 Scalar turbulence. *Nature* **405** (6787), 639–646.

SREENIVASAN, K. R. 1991 On local isotropy of passive scalars in turbulent shear flows. *Proc. R. Soc. Lond.* **434** (1890), 165–182.

SREENIVASAN, K. R. & ANTONIA, R. A. 1997 The phenomenology of small-scale turbulence. *Annu. Rev. Fluid Mech.* **29**, 435–472.

TAYLOR, R. J. 1958 Thermal structures in the lowest layers of the atmosphere. *Aust. J. Phys.* **11**, 168–176.

VENUGOPAL, V., ROUX, S. G., FOUFOULA-GEORGIOU, E. & ARNEODO, A. 2006 Revisiting multifractality of high-resolution temporal rainfall using a waveletbased formalism. *Water Resour. Res.* **42**, W06D14.

WARHAFT, Z. 2000 Passive scalars in turbulent flows. *Annu. Rev. Fluid Mech.* **32**, 203–240.

WATANABE, T. & GOTOH, T. 2004 Statistics of a passive scalar in homogeneous turbulence. *New J. Phys.* **6**.

XU, H., PUMIR, A., FALKOVICH, G., BODENSCHATZ, E., SHATS, M., XIA, H., FRANCOIS, N. & BOFFETTA, G. 2014 Flight-crash events in turbulence. *Proc. Natl Acad. Sci. USA* **111** (21), 7558–7563.

YAKHOT, V. 1997 Passive scalar advected by a rapidly changing random velocity field: probability density of scalar differences. *Phys. Rev.* E **55** (1, A), 329–336.

ZORZETTO, E., BRAGG, A. D. & KATUL, G. 2018 Extremes, intermittency, and time directionality of atmospheric turbulence at the crossover from production to inertial scales. *Phys. Rev. Fluid* **3**, 094604.